PHYSICAL REVIEW A **89**, 042704 (2014)

Electron-impact excitation and single- and multiple-ionization cross sections of heavy ions: Sn^{13+} as an example

P. F. Liu, Y. P. Liu, J. L. Zeng,* and J. M. Yuan
Department of Physics, College of Science, National University of Defense Technology, Changsha Hunan 410073, People's Republic of China

(Received 13 December 2013; published 28 April 2014)

The cross sections of electron impact with Sn^{13+} resulting in the production of Sn^{13+}-Sn^{16+} are investigated theoretically by using the fine-structure-level distorted-wave approximation from the threshold to 4000 eV. The electron-impact excitation, ionization, and resonant excitation processes are included in the cross sections. Contributions from different processes are determined by independent processes and isolated resonance approximations. The decay pathways and branching ratios for single and sequentially multiple autoionization for the final autoionized states are determined by detailed calculations. The cross section forming Sn^{13+} is the largest and next are those for Sn^{14+} and Sn^{15+}. The double-ionization cross section forming Sn^{15+} is smaller than that forming Sn^{14+}, yet the relative magnitude is larger at higher incident electron energy. A comparison with a recent measurement for the single-ionization cross section [A. Borovik, Jr. *et al.*, J. Phys. B **46**, 175201 (2013)] showed that accurate determination of the branching ratios for single and double autoionization and including contributions of the resonant excitation double autoionization are crucial to obtain accurate results.

DOI: 10.1103/PhysRevA.89.042704 PACS number(s): 34.80.Dp, 32.80.Hd

I. INTRODUCTION

Electron-ion collisions are among the most important atomic processes in hot plasmas. Accurate cross sections for electron-impact excitation, single ionization, and multiple ionization are important in plasma modeling in both astrophysical and laboratory plasmas [1–3]. Under conditions of collisional ionization equilibrium, the balance of electron-ion recombination and electron-impact single ionization (EISI) determines the charge state distribution (CSD). An accurate CSD, which in turn is determined by accurate cross sections, is very important in a wide regime of spectroscopic diagnostics to infer the physical conditions of plasmas such as the electron temperature, electron density, and elemental abundance [4,5]. In general, only EISI cross sections are needed to obtain the CSD for collisional ionization equilibrium plasmas. Yet in dynamic systems where the electron temperature changes rapidly, electron-impact double ionization and multiple ionization also play roles in the determination of the CSD [6]. The accuracy of the CSD and spectroscopic diagnostics depends on the underlying electron-impact ionization cross sections. Therefore, obtaining accurate electron-impact excitation and ionization cross sections is crucial in plasma modeling.

Accurate determination of the electron-impact excitation and ionization cross sections, however, is challenging work both experimentally and theoretically, especially for the heavy ions. Experimentally, for multielectron heavy ions, there is difficulty in producing well-characterized ground-state ion beams as most measurements of electron-impact ionization (EII) cross sections have been performed in a single-pass geometry in which metastable ions generally do not have enough time to radiatively relax to the ground state before measurements are performed [7,8]. Recently, experiments employing an ion storage ring were carried out [9–11], which allow the ions to be stored long enough for typically all metastable levels to radiatively relax before data acquisition begins. Yet these clean measurements are mainly limited on low-Z and middle-Z ions. At present, although some accurate experimental EII cross sections are used to obtain the rate coefficients, most such data are still derived by theory.

Theoretically, various methods such as close-coupling and distorted-wave methods were utilized to calculate the excitation and ionization cross sections [12–18]. Past theoretical work was mostly limited on separate excitation or ionization processes. For a complex many-electron heavy-ion system, electron-impact excitation and ionization to channels of autoionized states can give rise to multiple ionization to higher ionization stages. Several processes contribute to the excitation and ionization cross sections. For example, the EISI cross section is the sum of contributions from direct-ionization, excitation-autoionization (EA), and resonant excitation–double-autoionization (REDA) processes. The contributions from EA and REDA processes may involve complex Auger and radiative decay pathways. It is a troublesome work to accurately determine all relevant Auger and radiative decay pathways and their branching ratios including multiple ionization. Hence little theoretical research has been carried out to a complete understanding of all possible processes and multiple ionization, especially at high-energy electron-ion impact where many autoionized channels are involved.

In this work, we investigate the excitation, ionization, and resonant excitation processes of heavy ions by including all possible channels that will further autoionize to higher ionization stages, taking Sn^{13+} as an example. Accurate atomic data of Sn^{13+} along with other ionization stages of tin are of basic importance in understanding the physics of extreme ultraviolet (EUV) radiation light generation and transport and in optimizing EUV sources [19,20]. We [21] studied the radiative opacity of tin plasmas in the EUV region around 13.5 nm by using a detailed level accounting method [22–24]. Very recently, Borovik *et al.* [7] carried out a detailed experimental investigation of the electron-impact single-ionization cross sections of N-shell tin ions from the threshold up to 1000 eV.

---

*jlzeng@nudt.edu.cn

1050-2947/2014/89(4)/042704(10)

II. THEORETICAL METHOD

The calculations for the excitation and ionization cross sections were carried out by using a fine-structure-level distorted-wave approximation implemented by the flexible atomic code (FAC) developed by Gu [25]. A relativistic approach based on the Dirac equation is used throughout the entire package. The atomic structure is determined by diagonalizing the relativistic Hamiltonian of the ionic system. The basis states ϕ_j, which are referred to as configuration state functions (CSFs), are antisymmetric sums of the products of N one-electron Dirac spinors. An atomic state is approximated by a linear combination of CSFs with the same symmetry

$$\psi_i(J\pi) = \sum_j^{n_c} a_j \phi_j(J\pi), \tag{1}$$

where n_c is the number of CSFs and a_j denotes the representation of the atomic state in this basis.

The electron-impact excitation (EIE) cross section from the initial state ψ_i to the final state ψ_f can be expressed as

$$\sigma_{if} = \frac{2\pi}{k_i^2 g_i} \sum_{\kappa_i \kappa_f} \sum_{J_T} (2J_T + 1) \times \left| \langle \psi_i \kappa_i, J_T M_T | \sum_{p<q} \frac{1}{r_{pq}} | \psi_f \kappa_f, J_T M_T \rangle \right|^2, \tag{2}$$

where g_i is the statistical weight of the initial state, k_i is the kinetic momentum of the incident electron, κ_i and κ_f are the relativistic angular quantum numbers of the incident and scattered electrons, J_T is the total angular momentum when the target state is coupled to the continuum orbital, and M_T is the projection of the total angular momentum. The EII cross section, differential in the energy of the ejected electron, is obtained similarly from that of EIE by replacing one bound orbital in the final state with the free orbital of the ejected electron and summing over its angular momentum. Specifically, we investigate in detail the impact processes of the levels belonging to the ground configuration [Ne]$3l^{18}4s^2 4p^6 4d$ of Sn^{13+} with electrons including excitation, ionization, and resonant excitation processes from the threshold to 4000 eV. Here $3l^{18}$ means that the orbitals of $3d$, $3p$, and $3s$ are fully occupied. The cross sections resulting in the production of Sn^{13+}, Sn^{14+}, Sn^{15+} and Sn^{16+} are determined by summing over contributions from all possible processes. The electron-impact excitation processes of Sn^{13+} are shown schematically as

$$e^- + 3l^{18}4s^2 4p^6 4d \rightarrow \begin{cases} 3l^{18}4s^2 4p^6 nl + e^- \\ 3l^{18}4s^2 4p^5 4dnl + e^- \\ 3l^{18}4s 4p^6 4dnl + e^- \\ 3l^{17}4s^2 4p^6 4dnl + e^- \end{cases} \tag{3}$$

and the ionization processes as

$$e^- + 3l^{18}4s^2 4p^6 4d \rightarrow \begin{cases} 3l^{18}4s^2 4p^6 + 2e^- \\ 3l^{18}4s^2 4p^5 4d + 2e^- \\ 3l^{18}4s 4p^6 4d + 2e^- \\ 3l^{17}4s^2 4p^6 4d + 2e^-, \end{cases} \tag{4}$$

where $3l^{17}$ means that there are 17 electrons in the $3d$, $3p$, and $3s$ orbitals.

Resonant excitation processes play a role in the cross sections forming Sn^{13+} and Sn^{14+} ions via resonant excitation-autoionization (REA), REDA, and resonant excitation auto-double-ionization (READI) processes. These processes occur through dielectronic capture when an ion forms an autoionized state that subsequently decays by ejecting two electrons [2,26–31]. In the REDA process, the two electrons are released sequentially, whereas in READI the two electrons are ejected simultaneously. Specifically, the resonant excitation processes can be described as

$$e^- + 3l^{18}4s^2 4p^6 4d \rightarrow \begin{cases} 3l^{18}4s^2 4p^6 nln'l' \\ 3l^{18}4s^2 4p^5 4dnln'l' \\ 3l^{18}4s 4p^6 4dnln'l' \\ 3l^{17}4s^2 4p^6 4dnln'l'. \end{cases} \tag{5}$$

In the isolated resonance and independent process approximation, the dielectronic capture (DC) cross section can be obtained from the inverse Auger process by the detailed balance principle

$$\sigma_{ij}^{DC}(E) = \frac{\pi^2 \hbar^3}{m_e} \frac{g_j}{2 g_i E_{ij}} A_{ji}^a S(E), \tag{6}$$

where i and j represent the levels belonging to the ground configuration $3l^{18}4s^2 4p^6 4d$ of Sn^{13+} and the autoionized excited states of Sn^{12+}, respectively, E and E_{ij} are the incident electron energy and resonant energy, m_e is the mass of electron, g_i and g_j are the statistical weights of states i and j, A_{ji}^a is the Auger rate from j to i, and $S(E)$ is the resonant line profile. It is a Lorentzian profile if only the autoionization broadening is considered. In general, it is a Voigt function

$$S(E) = \frac{a}{\pi} \int_{-\infty}^{+\infty} \frac{e^{-x^2}}{a^2 + (v - x)^2} dx, \tag{7}$$

where

$$a = \sqrt{\ln 2}\, \Gamma_l / \Gamma_g, \tag{8}$$

$$v = \sqrt{\ln 2}(E - E_{ij}) / \Gamma_g, \tag{9}$$

where Γ_g and Γ_l are the Gaussian and Lorentzian (natural lifetime) half-width at half maximum (HWHM), respectively. The natural lifetime HWHM can be obtained from Auger rates by summing over all possible decay channels.

The total excitation cross section forming Sn^{13+} is the sum of contributions from excitation processes of Eq. (3) and resonant excitation processes of Eq. (5), which is given by

$$\sigma_{13-13} = \sum_i \sigma_i^{\text{exe}} + \sum_k \sigma_k^{DC} B_k^a, \tag{10}$$

where the summation of the first term is limited to those levels belonging to the bound states of Sn^{13+} and the single Auger branching ratios can be written as

$$B_k^a = \frac{\sum_{i<m} A_{ki}^a}{\sum_i A_{ki}^a + \sum_j A_{kj}^r}, \tag{11}$$

where A^a_{ki} and A^r_{kj} are the Auger and radiative decay rates from state k to i and j. Here $i < m$ denotes that only the truly bound levels belonging to Sn^{13+} are included in the summation. For a specific autoionized level k, there are in general many Auger decay pathways i. Some levels of the pathways are bound states whose energies are lower than the ionization potential (IP) of Sn^{13+}, while some are higher. The pathways with energies lower than the IP contributed to the cross section forming Sn^{13+}. Here $i < m$ means that only these pathways are included in the summation.

The total single-ionization cross section σ_{13-14} forming Sn^{14+} is given by

$$\sigma_{13-14} = \sigma_d + \sum_i \sigma_i^{\mathrm{exe}} B_i^a + \sum_k \sigma_k^{DC} B_k^{DA}, \tag{12}$$

where σ_d is the EII cross section contributed by those final levels belonging to the bound states of Sn^{14+}. The sequential double Auger branching ratios can be written as

$$B_k^{DA} = \left(\frac{\sum_l A^a_{kl}}{\sum_m A^a_{km} + \sum_n A^r_{kn}} \right) \left(\frac{\sum_f A^a_{lf}}{\sum_m A^a_{lm} + \sum_n A^r_{ln}} \right). \tag{13}$$

The double- and triple-ionization cross sections forming Sn^{15+} and Sn^{16+} can be obtained by summing contributions over relevant processes

$$\sigma_{13-15} = \sum_i \sigma_i^d B_i^a + \sum_k \sigma_k^{\mathrm{exe}} B_k^{DA} \tag{14}$$

and

$$\sigma_{13-16} = \sum_i \sigma_i^d B_i^{DA}. \tag{15}$$

In deriving the cross section forming Sn^{15+}, we do not include the contribution from the resonant excitation process since it is trivial compared with the other two processes. Similar consideration applies to the cross section forming Sn^{16+}.

III. RESULTS AND DISCUSSION

The first ionization potentials of Sn^{13+} and Sn^{14+} are calculated to be 281.86 and 379.16 eV, respectively, which are in good agreement with the experimental values of 281.9 and 379.0 eV [32]. According to our calculation, the energy thresholds are 348.91, 409.36, 784.00, 1016.38, and 1189.26 eV for the direct ionization of the Sn^{13+} $4p$, $4s$, $3d$, $3p$, and $3s$ subshells, respectively. The ionization potential of the $2p$ electron is 4238.05 eV, which is beyond the energy region of the present work. In the above processes of Eq. (4), the direct ionizations of $4d$, $4p$, and $4s$ result in Sn^{14+} as these final states are bound ones of Sn^{14+}. After enough relaxation time, they will decay to the ground states of Sn^{14+}. These processes contribute to the single-ionization cross section forming Sn^{14+}. The ionization of the $3d$ electron produces predominantly Sn^{15+}, which contributes to the double-ionization cross section, while the ionizations of the $3p$ and $3s$ electrons produce Sn^{16+} (triple ionization). The reason for this is that the $3d^{-1}$ levels will predominately autoionize to the bound levels of Sn^{15+}, while the $3p^{-1}$ and $3s^{-1}$ levels autoionize predominately to levels belonging to $3d^{-1}$ configurations, which will further autoionize to the bound levels of Sn^{16+}.

For the excitation processes, the case is a little different as the EIE to very high principal and angular quantum number nl is possible. The excitation of the $4d$ electron results in the formation of Sn^{13+}, while other orbitals produce ions of Sn^{13+}, Sn^{14+}, and Sn^{15+}, depending on the excitation to a different orbital nl. For the $4p$ and $4s$ electrons, excitations up to $6g$ basically form Sn^{13+}, yet to higher nl orbitals with $n \geqslant 7$ they form Sn^{14+} via EA, which occurs starting at the first ionization potential of 281.86 eV. The excitations from orbitals of $3d$ form predominantly Sn^{14+} via EA up to $n = 6$ and higher excitations of $n \geqslant 7$ form Sn^{15+} via excitation double autoionization. The excitations from orbitals of $3p$ and $3s$ produce predominantly Sn^{15+} via excitation double autoionization. We will give additional details on the branching ratios (BRs) for the single and double Auger processes below.

From the analysis of decay pathways, we know that the resonant excitation processes due to $4p$ and $4s$ produce Sn^{13+}, while those due to $3l$ processes produce Sn^{13+} and Sn^{14+}. The most important resonant channels for the single-ionization cross section are due to $3s^2 3p^6 3d^9 4s^2 4p^6 4dnln'l'$.

In the following, we first check the convergence of the excitation cross sections with nl. In this work, the maximal angular momentum l is taken to be 8; contributions from higher l proved to be trivial. In principle, the excitations up to very large n will contribute to the cross section, yet in reality the contribution decreases with an increase of n. Figure 1 shows the convergence behavior of the cross section with n for the excitation of $4d$, $4p$, $4s$, and $3d$. All possible contributions from different l are included. As there are two levels for the ground configuration of Sn^{13+}, the results shown in Fig. 1 are the configuration averaged values. Actually, the level-resolved cross section is very close to and basically the same value as the configuration averaged result. Note that a logarithmic scale is used for a clearer view of the cross section. The maximal n is calculated up to 30, with contributions from n = 4–10, 11–15, 16–20, 21–25, and 26–30 denoted by solid, dotted, dashed, dot-dashed, and dot–double-dashed lines, respectively. It can be seen that the results are fully converged for n up to 20. With an increase of n, the contributions decrease fast. For all the excitations, contributions from n = 4–10 dominate the cross section. The calculated cross section falls off as $1/n^3$ with increasing n. We use the excitation of the $4d$ electron as an example to quantitatively show such a trend. In Fig. 2 we give the $n^3\sigma_n$ as a function of incident electron energy for the excitation of $4d$ to principal quantum number $n = 5$, 9, 10, 15, and 25, where σ_n denotes the cross section contributed by the excitation of $4d$ to the nl ($l = 0,1,\ldots,n-1$) orbital. The excitations from $4p$, $4s$, $3d$, $3p$, and $3s$ orbitals show a similar trend with increasing n. The $1/n^3$ law holds for $n \geqslant 15$ for the excitations of all $4l$ and $3l$ electrons. Different n have different excitation thresholds and therefore such a $1/n^3$ law holds for different energy ranges. The common feature for σ_n is that the cross section first increases rapidly from the threshold and then slowly decreases over a wide energy range. From the energy with a maximal cross section to a higher energy range, the $1/n^3$ law holds. Obviously, the threshold is very close for high n. By assuming a valid formula of $1/n^3$ for extrapolation of

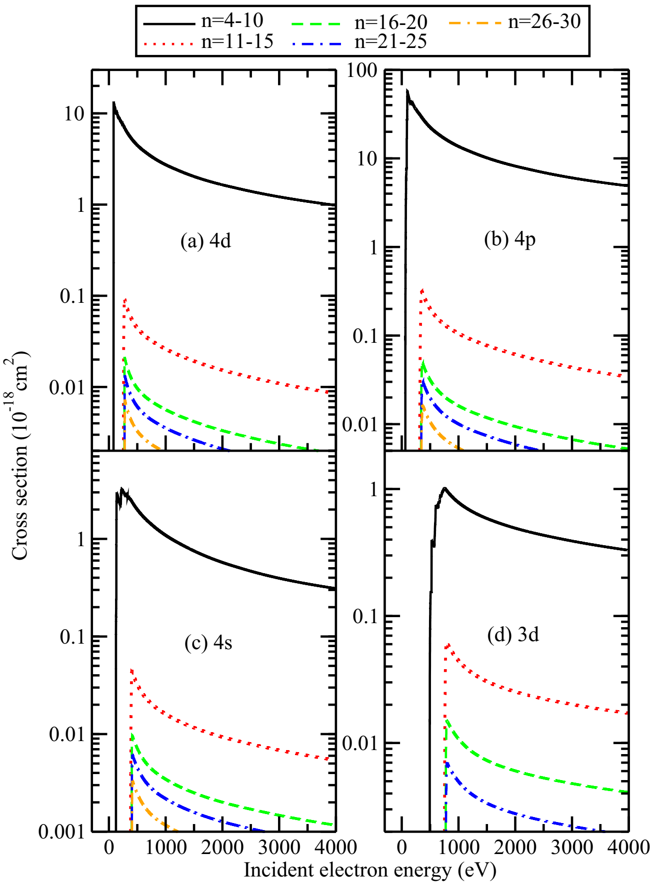

FIG. 1. (Color online) Convergence behavior of the cross section with n for the excitation of (a) $4d$, (b) $4p$, (c) $4s$, and (d) $3d$ subshells. The principal quantum number n is defined in Eq. (3) and contributions from all possible orbital angular momentum quantum numbers l have been included. The cross sections contributed by $n = 4$–10, 11–15, 16–20, 21–25, and 26–30 are given as solid, dotted, dashed, dot-dashed, and dot–double-dashed lines, respectively.

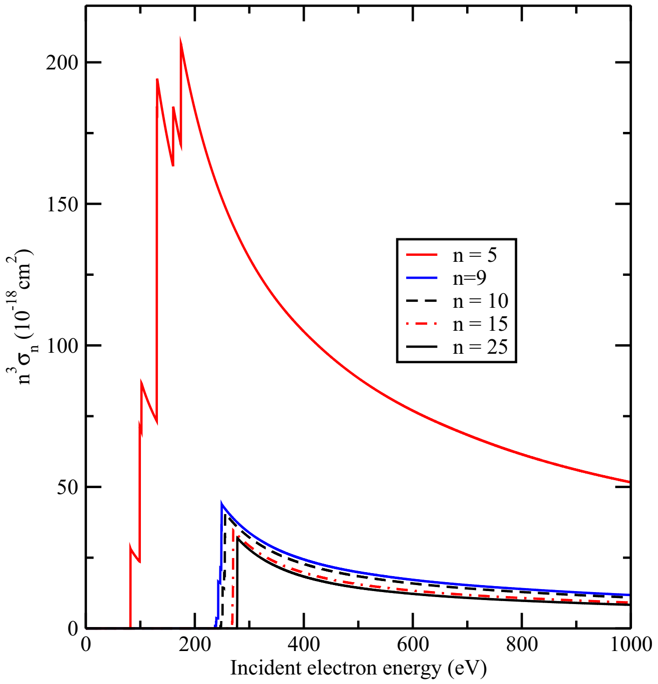

FIG. 2. (Color online) Plot of $n^3\sigma_n$ as a function of incident electron energy for the excitation of $4d$ to principal quantum number $n = 5, 9, 10, 15$, and 25 to verify the validity of the $1/n^3$ law for larger n. Here σ_n represents the cross section contributed by the excitation to all possible nl orbitals.

the cross section, the excitations to nl with $n > 30$ contribute to 0.16% of the total cross section.

The separate contributions from the EIE process forming Sn^{13+} (solid line), Sn^{14+} (dotted line), and Sn^{15+} (dashed line) are given in Fig. 3 for excitations of the $4d$, $4p$, $4s$, $3d$, $3p$, and $3s$ subshells. For clarity, a logarithmic scale is used in Figs. 3(a)–3(d) for the cross section, while a linear coordinate is used in Figs. 3(e) and 3(f). The cross sections forming Sn^{14+} and Sn^{15+} shown in Fig. 3 have been multiplied by the BR of the autoionization. There are a huge number of autoionization states for the final levels after excitation. They decay to higher ionization stages by single, double, or even triple Auger processes. To have a quantitative understanding of the BR for the involved excitations, we give two sets of BR data in Tables I and II. One set is for the excitation of the $4p$ electron and the other for $3d$. In Table I, the excitation energies, Auger rates, and BRs for the autoionization process are given for a few autoionized states with the lowest energy for the excitation of the $4p$ electron. The energies of these levels are just above the first ionization potential of Sn^{13+} (281.86 eV, calculated in this work). The levels belonging to $3l^{18}4s^24p^54d6s$, $3l^{18}4s^24p^54d6p$, and $3l^{18}4s^24p^54d6d$ are bound, while some of the levels from excitation of $6f$ and $6g$ are autoionized ones. There are 483 levels in total for the configurations of $4p$ excitation to $6f$, $6g$, and $6h$ orbitals and 380 of them are autoionized states. To obtain the BRs for the autoionized levels of $4p$ excitation to $6f$, $6g$, and $6h$ orbitals, we included configurations of $(3s^23p^63d^{10})4s^24p^64d$, $4s^24p^64f$, $4s^24p^65l$, $4s^24p^66l$, $4s^24p^54d^2$, $4s^24p^54d4f$, $4s^24p^54f^2$, $4s^24p^54d5l$, $4s^24p^54d6l$, $4s4p^64d^2$, $4s4p^64d4f$, $4s4p^64f^2$, $4s4p^64d5l$, $4s4p^64d6l$, $4s^24p^44d^3$, $4s^24p^44d^24f$, $4s4p^54d^3$, and $4s4p^54d^24f$ for Sn^{13+} in a complete configuration-interaction formalism to calculate the Auger decay rates and radiative transition probabilities. In calculating the radiative transition probabilities, care must be taken to ensure that all possible dipole-allowed transitions are included for any upper level in question. For the calculations of the Auger decay rates, it is necessary to include all possible decay pathways of Sn^{14+}, which is fulfilled by including configurations with one less electron than those of Sn^{13+}. From an inspection of Table I we know that the BRs vary considerably from a very small value of 0.0004 for level $[(4p_{3/2}^{-1}4d_{5/2})_2 6g_{9/2}]_{13/2}$ to nearly 1 (0.99) for $[(4p_{1/2}^{-1}4d_{3/2})_1 6f_{5/2}]_{7/2}$ and $[(4p_{3/2}^{-1}4d_{5/2})_2 6g_{9/2}]_{11/2}$, where full subshells are omitted in the designation of levels. The energy of the $4p$ excitation levels are in the range of 281.86–309.20 eV, which is smaller than that of the lowest excited states of Sn^{14+} (348.85 eV). As a result, they can only autoionize to the ground state of Sn^{14+}. From practical calculations, the radiative transition probability for the dipole-allowed transitions is basically on the order of 10^{11} s^{-1}, while the Auger decay rates vary dramatically from the order of 10^8 to 10^{14} s^{-1} for different levels. As the probability of dipole-allowed

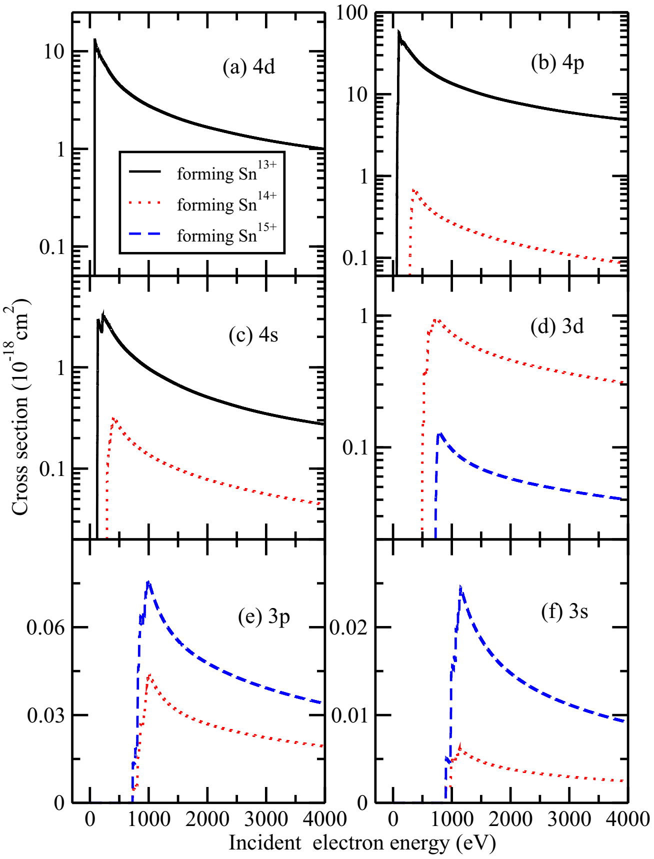

FIG. 3. (Color online) Separate contributions to the cross sections from electron-impact excitations of (a) $4d$, (b) $4p$, (c) $4s$, (d) $3d$, (e) $3p$, and (f) $3s$ subshells forming Sn^{13+} (solid line), Sn^{14+} (dotted line), and Sn^{15+} (dashed line).

transitions is far bigger than other types such as magnetic dipole and electric quadrupole transitions, only dipole-allowed transitions need to be included in the calculations of BRs. Thus it is not always a good approximation to assume that the BRs are equal to 1 in obtaining the cross section.

For the excitations from the $3l$ electron, the behavior of BRs is different. As illustrative examples, we give in Table II the BRs for the double Auger process from $3d$ excitation. These excited levels show a strong trend for autoionization with the Auger rates being on the order of 10^{13} s^{-1} and hence the Auger process dominates the radiative one for the decay. Such a characteristics is different from those levels belonging to $3l^{18}4s^24p^54d6l$. Furthermore, the excitation of the $3d$ electron to higher nl will result in the double Auger decay, including sequential cascade and direct processes. In Table II we give the excitation energies, total Auger rates, cascade double Auger decay (CDAD) rate, direct double Auger decay (DDAD) rate, and BRs for double autoionization. The DDAD rates are calculated according to the approximate formulas based on the knock-out and shake-off mechanisms [33,34]. Past work [35] showed that the DDAD process plays a role in atomic and low-charged ions. For a middle-charged ion such as Sn^{13+} its contribution should be trivial and negligible. It can be seen from Table II that the DDAD rates are indeed very small (<0.1%) compared with the total Auger rates. Moreover, the DDAD rates are also much smaller than the CDAD rates. This means that the contribution from READI is negligible in contrast to REDA. For excitation of the $3d$ electron to $4d$, $4f$, $5s$, $5p$, and $5d$ orbitals, the final levels predominantly decay to the bound states of Sn^{14+} with BRs for single autoionization being nearly 1. For excitation to the $5f$ orbital, some of the levels begin to have a small BR of a few thousandths for double autoionization. The energy threshold for double Auger decay is calculated to be 661.23 eV. For further excitation to the $7f$ orbital, most of the BRs for double autoionization increase up to 0.9. For these final levels belonging to the configuration of $3s^23p^63d^94s^24p^64d7f$, the dominating decay channels are levels of $3l^{18}4s^24p^57f$ and $3l^{18}4s^24p^44d7f$. The levels of the latter configuration will further autoionize to the bound states of Sn^{15+}.

From the above analysis we see that excitations of $4d$, $4p$, and $4s$ subshells can form Sn^{13+}, with the largest contribution from $4p$, next from $4d$, and the smallest from $4s$. Except for $4d$, other subshells of $4p$, $4s$, $3d$, $3p$, and $3s$ contribute to the

TABLE I. Excitation energy (in eV), single Auger decay rate (in s^{-1}), and single branching ratio (BR) of the autoionization for a few fine-structure levels belonging to the $4p$ excitation states of Sn^{13+} $3l^{18}4s^24p^54d6l$ ($l = f$ and g) with the lowest energy. Figures in square brackets in column 3 indicate powers of 10.

Level	Energy	Auger rate	BR
$[(4p_{1/2}^{-1}4d_{3/2})_16f_{5/2}]_{5/2}$	282.02	3.01[11]	0.82
$[(4p_{3/2}^{-1}4d_{5/2})_16f_{7/2}]_{7/2}$	282.08	7.74[10]	0.50
$[(4p_{3/2}^{-1}4d_{5/2})_26g_{9/2}]_{13/2}$	282.16	1.06[8]	0.0004
$[(4p_{3/2}^{-1}4d_{3/2})_26g_{7/2}]_{3/2}$	282.16	2.80[10]	0.093
$[(4p_{3/2}^{-1}4d_{5/2})_46g_{9/2}]_{9/2}$	282.24	5.36[13]	0.98
$[(4p_{3/2}^{-1}4d_{5/2})_26g_{9/2}]_{11/2}$	282.26	1.40[11]	0.34
$[(4p_{1/2}^{-1}4d_{3/2})_16f_{5/2}]_{7/2}$	282.28	9.59[12]	0.99
$[(4p_{3/2}^{-1}4d_{3/2})_36g_{7/2}]_{5/2}$	282.30	8.59[11]	0.75
$[(4p_{3/2}^{-1}4d_{5/2})_26g_{7/2}]_{9/2}$	282.38	7.89[12]	0.96
$[(4p_{3/2}^{-1}4d_{3/2})_36g_{9/2}]_{15/2}$	282.39	4.58[9]	0.019
$[(4p_{1/2}^{-1}4d_{3/2})_16f_{7/2}]_{9/2}$	282.40	2.51[12]	0.97
$[(4p_{3/2}^{-1}4d_{3/2})_36g_{7/2}]_{13/2}$	282.40	4.10[8]	0.0008
$[(4p_{1/2}^{-1}4d_{3/2})_16f_{7/2}]_{9/2}$	282.42	8.96[11]	0.87
$[(4p_{3/2}^{-1}4d_{5/2})_26g_{7/2}]_{7/2}$	282.44	1.54[11]	0.34
$[(4p_{1/2}^{-1}4d_{3/2})_16f_{5/2}]_{3/2}$	282.52	3.67[12]	0.98
$[(4p_{1/2}^{-1}4d_{3/2})_16f_{7/2}]_{5/2}$	282.53	2.24[12]	0.94
$[(4p_{1/2}^{-1}4d_{3/2})_16f_{7/2}]_{5/2}$	282.56	1.59[12]	0.90
$[(4p_{3/2}^{-1}4d_{5/2})_26g_{9/2}]_{11/2}$	282.56	3.20[13]	0.99
$[(4p_{3/2}^{-1}4d_{3/2})_36g_{7/2}]_{1/2}$	282.74	1.48[12]	0.84
$[(4p_{3/2}^{-1}4d_{3/2})_36g_{7/2}]_{11/2}$	282.83	1.46[13]	0.98
$[(4p_{3/2}^{-1}4d_{3/2})_26g_{9/2}]_{5/2}$	282.83	3.81[11]	0.53
$[(4p_{3/2}^{-1}4d_{3/2})_36g_{7/2})_{3/2}$	282.85	6.93[11]	0.70
$[(4p_{3/2}^{-1}4d_{5/2})_46g_{7/2}]_{7/2}$	282.87	3.15[11]	0.50
$[(4p_{3/2}^{-1}4d_{5/2})_46g_{7/2}]_{9/2}$	282.87	6.54[12]	0.95
$[(4p_{3/2}^{-1}4d_{5/2})_46g_{7/2}]_{5/2}$	282.92	4.33[10]	0.13
$[(4p_{3/2}^{-1}4d_{5/2})_46g_{7/2}]_{13/2}$	282.93	6.98[8]	0.0023
$[(4p_{3/2}^{-1}4d_{3/2})_36g_{7/2}]_{9/2}$	282.95	9.88[11]	0.76
$[(4p_{3/2}^{-1}4d_{5/2})_46g_{9/2}]_{15/2}$	282.97	1.33[9]	0.0042

TABLE II. Excitation energy (in eV), total Auger decay (AD) rate (in s^{-1}), sequential cascade double Auger decay (CDAD) rate, direct double Auger decay (DDAD) rate, and double autoionization branching ratio (DABR) for a few typical fine-structure levels belonging to the $3d$ excitation states of Sn^{13+} $3s^23p^63d^94s^24p^64dnl$. Figures in square brackets in columns 3–5 indicate powers of 10.

Level	Energy	AD rate	CDAD	DDAD	DABR
$[3d_{5/2}^{-1}(4d_{3/2}^2)_2]_{3/2}$	492.8	5.44[13]	0	0	0
$[(3d_{5/2}^{-1}4d_{5/2})_3 4f_{7/2}]_{3/2}$	580.1	5.05[13]	0	0	0
$[(3d_{3/2}^{-1}4d_{5/2})_3 5d_{5/2}]_{3/2}$	649.3	3.55[13]	0	0	0
$[(3d_{5/2}^{-1}4d_{3/2})_4 5f_{5/2}]_{13/2}$	662.5	4.66[13]	1.77[11]	1.16[10]	0.0041
$[(3d_{5/2}^{-1}4d_{3/2})_4 5g_{7/2}]_{5/2}$	675.7	5.18[13]	1.70[11]	1.22[10]	0.0035
$[(3d_{5/2}^{-1}4d_{3/2})_1 6d_{5/2}]_{7/2}$	683.8	5.27[13]	1.70[11]	3.87[10]	0.0039
$[(3d_{5/2}^{-1}4d_{3/2})_1 7s_{1/2}]_{3/2}$	700.0	4.89[13]	1.18[11]	8.30[10]	0.0041
$[(3d_{5/2}^{-1}4d_{3/2})_3 6f_{5/2}]_{5/2}$	702.5	4.16[13]	6.68[12]	7.08[10]	0.16
$[(3d_{5/2}^{-1}4d_{5/2})_4 6f_{7/2}]_{3/2}$	705.0	4.28[13]	3.15[12]	2.03[10]	0.074
$[(3d_{5/2}^{-1}4d_{3/2})_1 6g_{7/2}]_{9/2}$	707.5	5.16[13]	8.88[12]	1.08[11]	0.17
$[(3d_{5/2}^{-1}4d_{3/2})_1 6g_{9/2}]_{11/2}$	710.0	3.85[13]	6.41[12]	3.98[10]	0.17
$[(3d_{5/2}^{-1}4d_{3/2})_2 6g_{9/2}]_{11/2}$	712.5	3.56[13]	1.22[13]	2.11[10]	0.34
$[(3d_{3/2}^{-1}4d_{3/2})_1 7p_{1/2}]_{1/2}$	715.0	3.58[13]	7.47[12]	3.80[10]	0.21
$[(3d_{3/2}^{-1}4d_{3/2})_2 7p_{1/2}]_{3/2}$	717.5	3.07[13]	9.63[12]	9.84[9]	0.31
$[(3d_{3/2}^{-1}4d_{5/2})_4 6g_{9/2}]_{7/2}$	720.0	3.57[13]	1.45[13]	2.83[10]	0.41
$[(3d_{5/2}^{-1}4d_{3/2})_1 7f_{5/2}]_{3/2}$	722.6	4.87[13]	3.23[13]	1.83[11]	0.57
$[(3d_{5/2}^{-1}4d_{3/2})_2 7f_{5/2}]_{5/2}$	725.0	3.76[13]	3.24[13]	5.59[10]	0.86
$[(3d_{5/2}^{-1}4d_{5/2})_2 7f_{7/2}]_{1/2}$	727.5	3.57[13]	3.23[13]	3.28[10]	0.90
$[(3d_{5/2}^{-1}4d_{3/2})_2 7g_{9/2}]_{11/2}$	730.0	3.76[13]	3.22[13]	6.69[10]	0.86
$[(3d_{3/2}^{-1}4d_{5/2})_2 7f_{5/2}]_{11/2}$	735.1	3.11[13]	2.81[13]	4.10[10]	0.90
$[(3d_{3/2}^{-1}4d_{5/2})_4 7g_{9/2}]_{9/2}$	740.0	3.20[13]	2.81[13]	7.11[10]	0.88

cross section forming Sn^{14+}. Among these subshells, $3d$ has the largest cross section over the whole given energy range. Only excitation of $3d$, $3p$, and $3s$ subshells contributes to the cross section forming Sn^{15+}.

The cross sections forming Sn^{13+}, Sn^{14+}, and Sn^{15+} from the EIE processes of Eq. (3) are shown in Fig. 4 as black solid lines. The individually shaded areas show contributions of excitations involving the indicated subshells of $4d$, $4p$, $4s$, $3d$, $3p$, and $3s$. For clarity, a logarithmic scale is used in Fig. 4(a) for the cross section, while a linear coordinate is used in Figs. 4(b) and 4(c). We can see that the cross section forming Sn^{13+} is more than an order of magnitude larger than that of Sn^{14+} at higher incident electron energy, while that forming Sn^{15+} is nearly an order of magnitude smaller than that of Sn^{14+}. Excitation of subshells of $4p$ and $4s$ contribute mainly to cross sections forming Sn^{13+} and Sn^{14+}, while excitation of $4d$ only contributes to Sn^{13+}. Excitation of subshells of $3p$ and $3s$ produce mainly Sn^{15+}, while $3d$ contributes to both Sn^{14+} and Sn^{15+}. In Fig. 4(b) we also give the cross section forming Sn^{14+} by assuming the BR to be 1 (dotted line). The effects of the BR are clearly seen, especially near the threshold.

For the EII processes given in Eq. (4), the cross sections forming Sn^{14+}, Sn^{15+}, and Sn^{16+} are given in Fig. 5 as solid, dotted, and dashed lines, respectively. The BRs for the single and double autoionization forming Sn^{15+} and Sn^{16+} have been considered. The ionization of $4d$, $4p$, and $4s$ electrons only form Sn^{14+}, while the ionization of $3d$, $3p$, and $3s$ electrons can further decay to Sn^{15+} or even Sn^{16+} by double and triple ionization. The detailed decay pathways for the ionization of $3l$ electron can be determined in the same way as for excitation. For simplicity, we do not give any details here. From an inspection of Fig. 5 one can see that the ionization thresholds increase with higher ionization stages and the cross section forming Sn^{16+} is far smaller than those of Sn^{14+} and Sn^{15+}. With an increase of incident electron energy, the relative cross section forming Sn^{15+} is larger than that of Sn^{14+}. At an incident electron energy of 1500 eV, the cross section forming Sn^{14+} is about two times larger than that forming Sn^{15+}, while it is only 50% larger at 4000 eV.

To obtain the resonant excitation cross section contributed by the processes of Eq. (5), we include $nl = 4d$, $4f$, and $5l - 8l$ and $n'l' = 4d, 4f$, and $5l' - 25l'$ with all possible l and l'. The excitations from $4s$, $4p$, and $4d$ electrons predominantly contribute to the excitation cross section forming Sn^{13+}, while those of $3s$, $3p$, and $3d$ predominantly contribute to the single-ionization cross section forming Sn^{14+}. We give excitation of $3s^23p^63d^94s^24p^64dnln'l'$ from the $3d$ electron as an example to illustrate the computational details. As there are too many levels in these configurations, we carried out nine separate calculations to obtain the cross section. One such calculation includes resonant excitations of $3s^23p^63d^94s^24p^64dnln'l'$ with $nl = 4d$ and $n'l' = 4d, 4f, 5l'$ ($l' = 0,1,2,3,4$). The interaction between all these configurations is included to obtain the level energies, Auger decay rates, and autoionization widths of these autoionized levels. All these quantities are needed in the calculation of the dielectronic capture cross section given

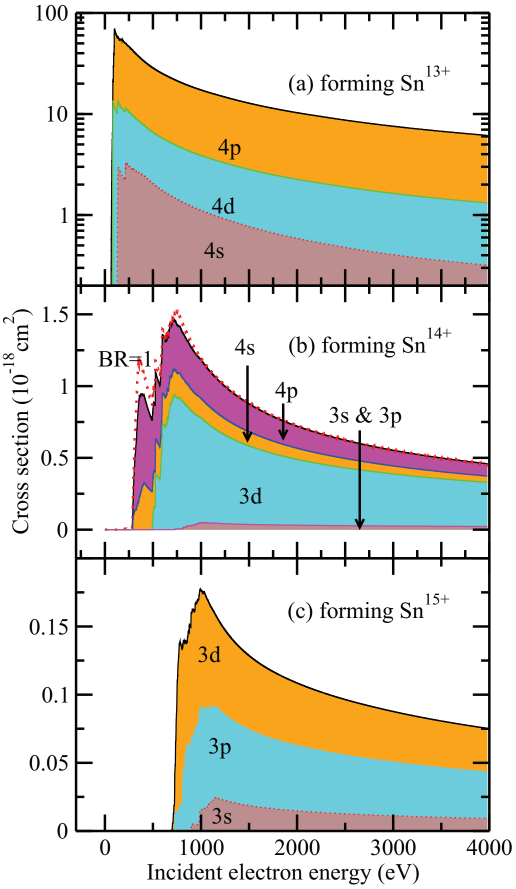

FIG. 4. (Color) Cross sections forming (a) Sn^{13+}, (b) Sn^{14+}, and (c) Sn^{15+} from electron-impact excitation processes of Eq. (3) (black solid lines). (b) Results found by assuming that the BR equals 1 (red dotted line). Contributions from different subshells of $4d$, $4p$, $4s$, $3d$, $3p$, and $3s$ are given by the individually shaded areas.

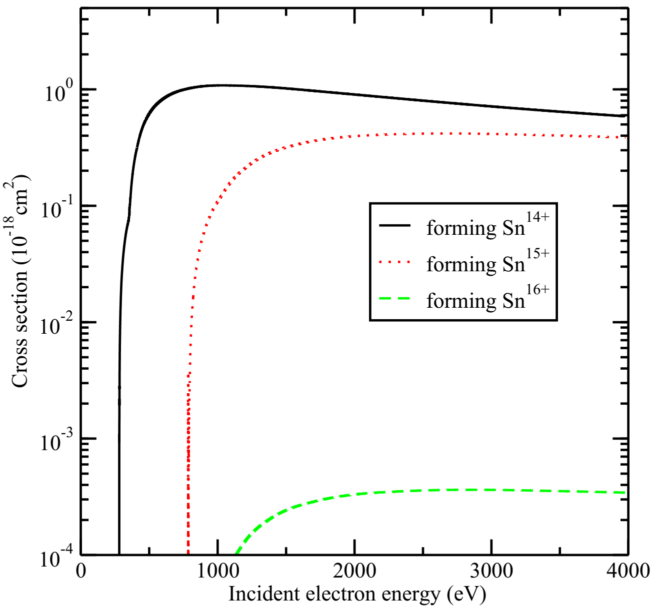

FIG. 5. (Color online) Cross sections forming Sn^{14+}, Sn^{15+}, and Sn^{16+} from the ionization processes of Eq. (4).

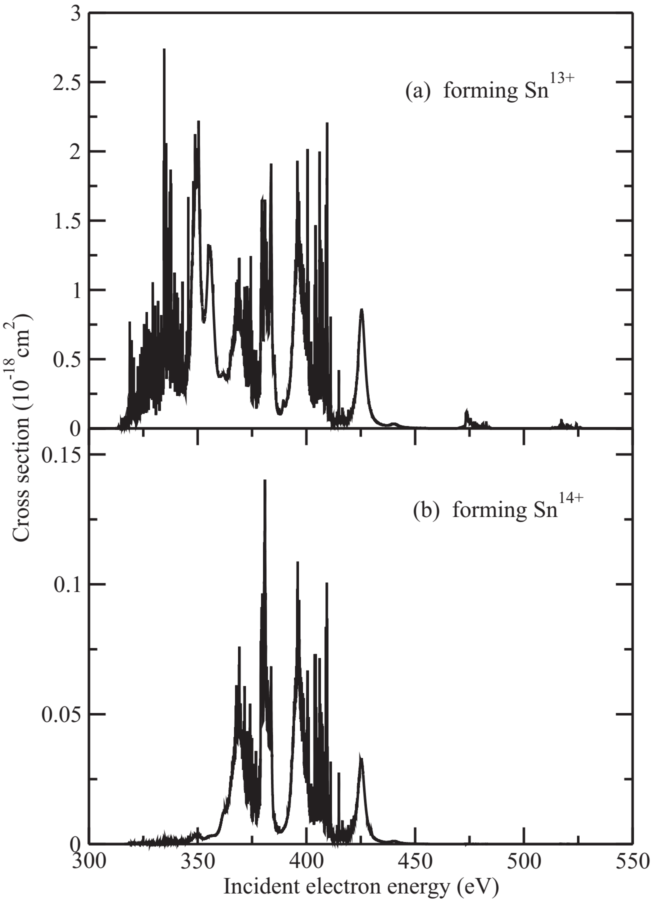

FIG. 6. Cross sections forming (a) Sn^{13+} and (b) Sn^{14+} contributed by the resonant excitation process from $3d$ autoionized levels belonging to configurations of $3s^23p^63d^94s^24p^64d^2nl$ ($nl = 4d, 4f, 5s, 5p, 5d, 5f$, and $5g$). Only autoionization broadening is considered for the resonant line profile.

in Eq. (6). In obtaining these data, we carried out a calculation for the Auger decay rate of these resonant states of Sn^{12+} by using the FAC software implemented by a distorted-wave approximation. The atomic structure for Sn^{12+} included the ground configuration $3s^23p^63d^{10}4s^24p^64d^2$ and those of single and double excitation from $4d$, $4p$, and $4s$ orbitals of the ground configuration to $n'l' = 4d,4f,5l'$ ($l' = 0,1,2,3,4$), as well as those mentioned above for excitation of the $3d$ electron. A similar scale of configurations applies for the atomic structure of Sn^{13+}. Figure 6 shows the calculated cross section forming Sn^{13+} and Sn^{14+} obtained using this set of resonant states. Contributions from all other resonant excitations can be derived in the same way.

The total cross sections from the ground configuration of Sn^{13+} forming Sn^{13+}, Sn^{14+}, Sn^{15+}, and Sn^{16+} are summarized in Fig. 7 by summing all possible processes considered above. The contributions from the EIE, EII, and resonant excitation processes are denoted in the figure by individually shaded areas. The cross sections around resonant excitations are expanded in the insets of Figs. 7(a) and 7(b) for a clearer view. In obtaining the cross section of the resonant excitation process, an instrumental resolution of 2.0 eV has been assumed. In principle, it is not necessary to consider

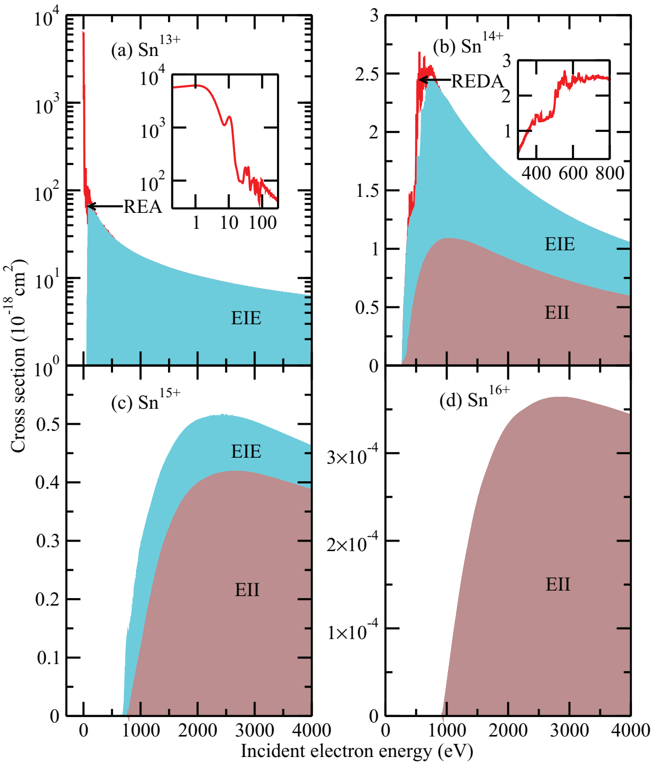

FIG. 7. (Color) Total cross sections forming (a) Sn^{13+}, (b) Sn^{14+}, (c) Sn^{15+}, and (d) Sn^{16+} from the processes of EIE (blue shaded areas), EII (brown shaded areas), and resonant excitation of REA and REDA (red lines).

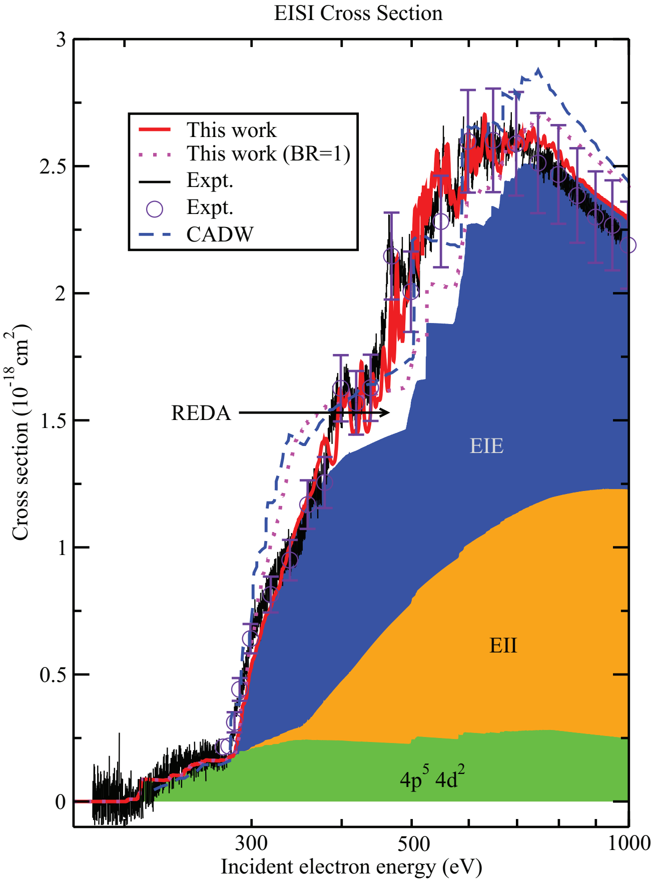

FIG. 8. (Color) Present calculated single-ionization cross section of Sn^{13+} compared with experimental results by Borovik *et al.* [7] (black solid line) and CADW calculations (blue dashed line). A fraction of 7.5% is assumed for the excited levels belonging to the configuration of $3l^{18}4s^24p^54d^2$ and its contributions to the cross section are shown as a green shaded area at the bottom. Contributions from the EII and EIE processes are represented as orange and blue shaded areas. The area between the upper line of the blue area and the red solid line is contributed by the REDA process. The open circles give representative experimental data with the error bars. The red dotted line shows the cross section from the EII and EIE processes by assuming that the BR equals 1 for the EIE.

the instrumental broadening in our theoretical work. In order to compare with the experimental results, however, one has to take the instrumental resolution into account. A value of 2.0 eV for the instrumental resolution is estimated from the experimental work of Borovik *et al.* [7], with which we will compare our theoretical result in the following. Borovik *et al.* [7] did not give the exact instrumental resolution in their work and hence we have to deduce this value by comparing our result with the measurement. The resonant process dominates the cross section forming Sn^{13+} at very small incident electron energy. The REDA has a definite contribution for the formation of Sn^{14+}. For example, it effectively enhances the cross section from 1.9 to 2.5 Mb at an incident energy of around 540 eV. With an increase of incident energy, the relative cross section forming Sn^{15+} is larger than that forming Sn^{14+}. The cross section contributed by the READI process is negligible, in contrast to that of REDA as the DDAD rate is indeed very small compared with the total Auger rate, just as we have discussed in the EIE process. Over the whole energy range, the cross section forming Sn^{16+} is very small compared with other ionization stages.

In order to check the accuracy of present work, our calculated single-ionization cross section of Sn^{13+} (red solid line) is compared in Fig. 8 with the experimental results (black solid line) carried out by Borovik *et al.* [7] in the energy range from the threshold up to 1000 eV. Open circles shows representative absolute cross section data measured by Borovik *et al.* [7], with the error bars being given. To obtain the result, we assumed a fraction of 7.5%, which is estimated by the experiment [7], for the excited levels belonging to the configuration of $4p^54d^2$. Thus the cross section is obtained from the single-ionization cross section of the ground configuration $4p^64d$ times 0.925 plus the single-ionization cross section of the configuration $4p^54d^2$ times 0.075. The contribution from the levels of the excited configuration is depicted in the lowest shaded area of the figure. The method used for the calculation of the cross section of $4p^54d^2$ is the same as that used for the ground configuration. The separate contributions from the EII (orange), EIE (blue), and REDA processes are shown explicitly by individually shaded areas. It can be seen that very good agreement is obtained between our theory and experiment over the whole given incident electron energy range. This elucidates the role of the resonant excitation for the complex heavy ion of Sn^{13+}. For comparison, the theoretical result obtained by using a configuration-averaged distorted-wave (CADW) method is also given as a blue dashed line. The CADW formalism was implemented in the Los Alamos National Laboratory Atomic Physics Code Package [36]. In those CADW calculations, contributions from only EII and EIE processes were included. Moreover, in calculating the contribution of EIE, the BR for the autoionization is assumed to be 1. To see the effects of the BR, we also carried out calculations by assuming the BR to be 1. Our fine-structure calculations obtained the result shown by a red dotted line by including contributions from the EII and EIE processes. Obviously, the effects of an accurate BR are evident in the whole energy range, especially in energy region of 300-500 eV and above 800 eV. The reason for this difference is that the BR deviates from 1, which means accurate determination of the Auger and radiative decay pathways is important in accurately calculating the cross section. In the region of 300–500 eV, the radiative processes play a larger role than in other energy ranges and therefore decrease the BR. In the energy region above 700 eV, sequential double ionization plays a role, also resulting in a decrease of the BR. From a comparison of the theoretical results shown by dashed and dotted lines, we can see that the CADW calculations predicted a cross section larger than ours. Note also that our calculations included EIE from contributions of much higher nl (up to $n = 30$), while the CADW calculations only included contributions from maximal nl up to $11i$. The CADW cross section exceeds the experimental results in the energy range from approximately 300 up to 390 eV mainly due to the neglect of the accurate calculation of the BR in the EIE process involving the $4p$ and $4s$ subshells.

From the above comparison, we can see that all major physical effects should be considered to obtain accurate ionization cross sections. For Sn^{13+}, only including the contributions from the EII and EIE processes is not enough to interpret the experiment [7]. Resonant excitation double autoionization plays a definite role in the total single-ionization cross section. Only when we include its contribution in the cross section can we obtain excellent agreement with the experiment. The physical effects due to REDA were investigated theoretically [29–31] and experimentally [37]. Borovik *et al.* [7] used the measured cross section in the energy range from the threshold up to 1000 eV and extrapolated theoretical data to obtain the plasma rate coefficients. Combining their measured data and our theoretical cross sections up to a higher incident electron energy, we believe that more accurate plasma rate coefficients due to electron-impact processes can be obtained. Our work shows that accurate treatment of all relevant atomic processes is vital in obtaining accurate electron-impact ionization rate coefficients.

In the above calculations, we only considered the indirect process related to the excitation and ionization of a single inner-shell electron of Sn^{13+} followed by single and multiple autoionization. We did not include the direct-multiple-ionization process where the incident electron ejects two or three of the bound electrons to form the more highly charged ions. Such a direct-multiple-ionization process does not contribute to the single-ionization cross section, yet it may affect the double- and triple-ionization cross sections and thus brings into question the accuracy of multiple-ionization cross sections. Calculating the cross section of the direct-triple-ionization process is too complicated and beyond this work. In the following we restrict our discussion to the electron-impact direct-double-ionization process. This process has the following basic and general features. First, cross sections for light atoms are dominated by the direct double ionization, yet those for medium to heavy atoms are generally dominated by the indirect process from inner-shell ionization [38,39]. Second, there are two generally agreed upon mechanisms of knock-out and shake-off for the direct double process of electron impact [40], just as for the direct double Auger decay process [33,34]. Both mechanisms are due to the interaction of electrons, which means that the electron correlation is the main reason for the direct-double-ionization process. It is well known that the effects of electron correlation are much more pronounced for neutral atoms and low-charged ions than the highly charged ions. Therefore, it can be reasonably deduced that the direct-double-ionization cross section is smaller than the indirect one for 13-fold ionized Sn^{13+}.

Practical calculations are needed to prove the above statement, which remains a challenging computational task for such Coulomb four-body problems, in particular relating to heavy ions. Very few *ab initio* calculations have been carried out for the four-body process [41,42]. Pindzola *et al.* [41,42] developed a time-dependent close-coupling method to calculate the direct double ionization of atomic and ionic systems with two valence electrons in the ns orbital with n being 2–4. Time-dependent close coupling is one of the most accurate theoretical formalisms to treat such four-body problems. However, few reports are found for more complicated atomic or ionic systems with more valence electrons. In this work, we estimated the direct-double-ionization cross section according to the simplified approximate formalism deduced from the knock-out and shake-off mechanisms, just as we did in the treatment of the direct double Auger decay process [33,34]. The computational details are not the main focus of the present work and thus are not given here. Practical calculations show that near the direct-double-ionization threshold and around the peak cross section, the knock-out mechanism plays a dominant role in the direct-double-ionization cross section. The contribution from the shake-off mechanism is about two orders of magnitude smaller than that from the knock-out mechanism. The maximal direct-double-ionization cross section from contributions from both mechanisms is determined to be only 1.5 kb ($1\mathrm{kb} = 10^{-21}\ \mathrm{cm}^2$), which is more than two orders of magnitude smaller than that of the indirect-double-ionization cross section. The direct-triple-ionization cross section should be even much smaller. Therefore, the cross sections contributed by the direct double and triple processes are negligible compared with those of indirect ones.

The accuracy obtained by the FAC code [25] was discussed in detail by Gu in the software used in Ref. [25]. Briefly, the accuracy is nearly the same as that of the multiconfiguration Dirac-Fock method for positively charged ions, yet it is much worse for the neutral atoms. The accuracy problem was also discussed in the evaluation of autoionization and dielectronic capture rates used in collisional-radiative models by an analytical formula of Au^{50+} [43]. For the middle-charged ion Sn^{13+}, we estimated that the accuracy should be better than 20% for the single- and double-ionization cross sections. Such a conclusion is verified for the single-ionization cross section when compared with the experiment. For the triple-ionization cross section, however, it may be a little worse.

IV. CONCLUSION

The electron-impact processes of Sn^{13+} including excitation, ionization, and resonant excitation have been systematically studied theoretically. The cross sections forming Sn^{13+}, Sn^{14+}, Sn^{15+}, and Sn^{16+} ions were calculated using the fine-structure-level distorted-wave approximation from the threshold to 4000 eV. By analyzing the pathways of the Auger and radiative decay of the final levels, we determined the relative contributions of different mechanisms to the cross sections. For the excitation and ionization processes, sequential multiple Auger decay up to two higher ionization stages is possible. For the single ionization forming the Sn^{14+} ion, the contribution from the resonant excitation process plays a role in the cross section. The direct-double-ionization cross section is negligibly small compared with that of the indirect process. Accurate determination of the branching ratios of autoionization and the cross section from the resonant excitation process are crucial in interpreting the recent experimental measurement and determining the plasma rate coefficients.

ACKNOWLEDGMENTS

This work was supported by the National Natural Science Foundation of China under Grants No. 11274382, No. 11274383, and No. 11204376.

---

[1] T. R. Kallman and P. Palmeri, Rev. Mod. Phys. **79**, 79 (2007).
[2] A. Müller, Adv. At. Mol. Opt. Phys. **55**, 293 (2008).
[3] J. Y. Dai, Y. Hou, and J. M. Yuan, Phys. Rev. Lett. **104**, 245001 (2010).
[4] E. Landi and M. Landini, Astron. Astrophys. **347**, 401 (1999).
[5] P. Bryans, E. Landi, and D. W. Savin, Astrophys. J. **691**, 1540 (2009).
[6] A. Müller, Phys. Lett. A **113**, 415 (1986).
[7] A. Borovik, Jr., M. F. Gharaibeh, P. M. Hillenbrand, S. Schippers, and A. Müller, J. Phys. B **46**, 175201 (2013).
[8] A. Borovik, Jr., C. Brandau, J. Jacobi, S. Schippers, and A. Müller, J. Phys. B **44**, 205205 (2011).
[9] M. Hahn, A. Becker, D. Bernhardt, M. Grieser, C. Krantz, M. Lestinsky, A. Müller, O. Novotny, R. Repnow, S. Schippers, K. Spruck, A. Wolf, and D. W. Savin, Astrophys. J. **767**, 47 (2013).
[10] M. Hahn, M. Grieser, C. Krantz, M. Lestinsky, A. Müller, O. Novotny, R. Repnow, S. Schippers, A. Wolf, and D. W. Savin, Astrophys. J. **735**, 105 (2011).
[11] M. Hahn, D. Bernhardt, M. Grieser, C. Krantz, M. Lestinsky, A. Müller, O. Novotny, R. Repnow, S. Schippers, A. Wolf, and D. W. Savin, Astrophys. J. **729**, 76 (2011).
[12] D. L. Moores and K. J. Reed, Adv. At. Mol. Opt. Phys. **34**, 301 (1994).
[13] P. Burke, C. Nobel, and V. Burke, in *Advances in Atomic, Molecular, and Optical Physics*, edited by P. Berman, C. Lin, and E. Arimondo (Elsevier, Amsterdam, 2006), pp. 237–318.
[14] D. C. Griffin and M. S. Pindzola, Adv. At. Mol. Opt. Phys. **54**, 203 (2006).
[15] K. Wang, J. Yan, M. Huang, C. Y. Li, J. L. Zeng, C. Y. Chen, Y. S. Wang, and Y. M. Zou, At. Data Nucl. Data Tables **98**, 779 (2012).
[16] F. Li, G. Y. Liang, M. A. Bari, and G. Zhao, Astron. Astrophys. **556**, A32 (2013).
[17] G. Y. Liang, N. R. Badnell, and G. Zhao, Astron. Astrophys. **547**, A87 (2012).
[18] J. L. Zeng, G. Zhao, and J. M. Yuan, At. Data Nucl. Data Tables **93**, 199 (2007).
[19] W. Svendsen and G. O'Sullivan, Phys. Rev. A **50**, 3710 (1994).
[20] U. Stamm, J. Phys. D **37**, 3244 (2004).
[21] J. L. Zeng, C. Gao, and J. M. Yuan, Phys. Rev. E **82**, 026409 (2010).
[22] J. L. Zeng and J. M. Yuan, Phys. Rev. E **74**, 025401(R) (2006).
[23] J. L. Zeng and J. M. Yuan, Phys. Rev. E **76**, 026401 (2007).
[24] J. L. Zeng, J. Phys. B **41**, 125702 (2008).
[25] M. F. Gu, Can. J. Phys. **86**, 675 (2008).
[26] K. J. LaGattuta and Y. Hahn, Phys. Rev. A **24**, 2273 (1981).
[27] A. Müller, K. Tinschert, G. Hofmann, E. Salzborn, and G. H. Dunn, Phys. Rev. Lett. **61**, 70 (1988).
[28] A. Müller, G. Hofmann, K. Tinschert, and E. Salzborn, Phys. Rev. Lett. **61**, 1352 (1988).
[29] M. H. Chen, K. J. Reed, and D. L. Moores, Phys. Rev. Lett. **64**, 1350 (1990).
[30] T. M. Shen, C. Y. Chen, Y. S. Wang, Y. M. Zou, and M. F. Gu, Phys. Rev. A **76**, 022703 (2007).
[31] T. M. Shen, C. Y. Chen, Y. S. Wang, Y. M. Zou, and M. F. Gu, J. Phys. B **40**, 3075 (2007).
[32] Y. Ralchenko *et al.*, NIST Atomic Spectra Database (NIST, Gaithersburgh, 2008), http://physics.nist.gov/asd3.
[33] J. L. Zeng, P. F. Liu, W. J. Xiang, and J. M. Yuan, Phys. Rev. A **87**, 033419 (2013).
[34] J. L. Zeng, P. F. Liu, W. J. Xiang, and J. M. Yuan, J. Phys. B **46**, 215002 (2013).
[35] W. J. Xiang, C. Gao, Y. S. Fu, J. L. Zeng, and J. M. Yuan, Phys. Rev. A **86**, 061401(R) (2012).
[36] Atomic and Optical Theory Group, Los Alamos National Laboratory Atomic physics codes package, http://aphysics2.lanl.gov/cgi-bin/ION/runlanl108d.pl and http://aphysics2.lanl.gov/tempweb/lanl/.
[37] J. Linkemann, A. Müller, J. Kenntner, D. Habs, D. Schwalm, A. Wolf, N. R. Badnell, and M. S. Pindzola, Phys. Rev. Lett. **74**, 4173 (1995).
[38] M. S. Pindzola, J. A. Ludlow, F. Robicheaux, J. Colgan, and D. C. Griffin, J. Phys. B **42**, 215204 (2009).
[39] M. S. Pindzola, D. C. Griffin, C. Bottcher, D. H. Crandall, R. A. Phaneuf, and D. C. Gregory, Phys. Rev. A **29**, 1749 (1984).
[40] I. L. Beigman, J. Exp. Theor. Phys. **102**, 577 (2006).
[41] M. S. Pindzola, C. P. Ballance, F. Robicheaux, and J. Colgan, J. Phys. B **43**, 105204 (2010).
[42] M. S. Pindzola, J. A. Ludlow, C. P. Ballance, F. Robicheaux, and J. Colgan, J. Phys. B **44**, 105202 (2011).
[43] C. Gao and J. L. Zeng, Phys. Rev. A **82**, 062515 (2010).